Deep learning-based approach for delamination identification using animation of Lamb waves propagation

Saeed Ullah*

Institute of Fluid-Flow Machinery, Polish Academy of Sciences
14 Fiszera Street, 80-231, Gdansk, Poland

Abstract

Composite materials are prone to various kinds of defects in their service life, among which delamination is a very hazardous type of damage. The traditional visual inspection techniques often fail to detect delamination in composite structures. Guided Lamb waves are increasingly being applied for the identification of delamination in these structures. Scanning laser Doppler vibrometry can measure the full wavefield of guided Lamb waves, such full wavefield contains rich information about defects. In this research work, a novel deep learning-based semantic segmentation technique is applied for delamination identification on full wavefield data. A big dataset of full wavefield images resulting from the interaction with delamination of random shape, size, and location was utilised and fed into the proposed deep learning model. The main motive of this research work is to investigate the applicability of deep learning-based approach for delamination identification in composite structures by using only the animations of guided Lamb waves. It is verified that the performance of the proposed deep learning model is good. Moreover, it enables better automation of identification of delamination, which can further produce damage maps without the intervention of the user. Furthermore, the developed deep learning model also indicates the capability of generalising well to the experimental data.

Keywords: Lamb waves; Delamination identification; Semantic segmentation; Deep learning; ConvLSTM

1 Introduction

These days, composite materials are extensively used for acquiring the desired performance in a broad range of industries, such as aerospace, wind turbines, automotive, marine, and many more. This extensive use of composite materials is due to their considerable advantages, such as lightweight, low cost, high strength, higher stiffness-to-mass ratio compared to metals, and effective corrosion resistance [1–3]. However, these materials are prone to different kinds of defects such as cracks, fiber breakage, debonding, and delamination [3, 4]. Among these defects, delamination is one of the most hazardous forms

---

of defects in composite materials. Delamination diminishes the life of these structures and can lead to catastrophic failures if not detected at an early stage [4, 5]. Therefore, for the safe operation of these structures, it is essential to identify the delamination effectively.

The detection of delamination in composite materials is very challenging for conventional visual inspection techniques because it occurs between plies of composite laminate and is invisible from external surfaces [6, 7]. Accordingly, different types of nondestructive testing (NDT) and structural health monitoring (SHM) techniques have been proposed for delamination identification in composite structures. Among various damage identification techniques, ultrasonic guided waves are widely known as one of the most promising techniques for the quantitative identification of defects in composite structures. The widespread applications of these waves are due to their higher sensitivity to small defects, propagation with low attenuation, and potential to monitor large areas and the need of only a small number of sparsely distributed transducers [8–10].

However, utilising a smaller number of transducers is not appropriate for acquiring high-quality resolution damage maps and the assessment of damage size. On the other hand, the employment of a very dense array of transducers is also not feasible in most situations. To alleviate such problems, a scanning laser Doppler vibrometer (SLDV) is employed. SLDV is capable of measuring the propagation of guided waves in a highly dense grid of points over the surface of a large specimen. This collection of signals is known as full wavefield [11]. In recent years, full wavefield signals have been used for the detection and localisation of defects in composite structures [11–14]. Damage identification techniques employing full wavefield signals are capable of effectively estimating not only the location but also the size of damage [12, 13]. Full wavefields provide valuable information regarding the interaction of guided Lamb waves with potential defects. However, these full wavefields are very complex. Analysing such wavefields is very difficult for conventional physics or classical machine learning-based models.

Conversely, deep learning, which is originated from the artificial neural network (ANN), is capable of handling such complex and nonlinear data and has shown very promising results in different domains such as computer vision, object detection, speech recognition, remote sensing, medical sciences, and many more [15–17]. In recent years, deep learning has also shown significant improvements in image segmentation due to the advancement of deep convolutional neural networks (CNNs). Deep learning-based systems intend to derive hierarchical representations from the input data via constructing deep neural networks with multiple layers of non-linear transformations. In deep learning architectures, the output of one layer acts as the input to the next subsequent layer. The stacking composition of many layers enables the model to learn complex patterns from raw input data. Therefore, these systems do not need extensive human labour and knowledge for hand-crafted feature design [18].

Different researchers have applied basic ANN and deep learning architectures for damage identification in composite structures by employing thermography, vibration, and frequency-based approaches [19–22]. Furthermore, many researchers have also applied ANN and deep learning-based approaches for damage identification in composite structures by utilising guided Lamb waves [23–30].

In this work, the author applied a deep learning model on the full wavefield frames of propagating Lamb waves. This means that there is no need of any signal post-processing technique like for example RMS. Consequently, a many-to-one prediction scheme (many input frames to damage map) was used in the proposed deep learning model. In simple words, a sequence of full wavefield frames (animation) is fed into the proposed deep learning model. The proposed model is inspired by convolutional long short-term mem-

ory (ConvLSTM) architecture and tailored to the particular problem of delamination identification. Two classes (damaged and undamaged) were defined in the pixel-wise segmentation problem.

To the best of the author knowledge, it is the first implementation of deep neural networks utilising Lamb wave propagation animations for damage imaging with semantic segmentation. The proposed model showed excellent capabilities to identify the delamination in the numerically generated dataset. Moreover, the developed model can generalise well, therefore, the proposed model could be used for delamination identification in real-world scenarios. This is confirmed through the experiments on CFRP plates with single and multiple delaminations.

2   Image segmentation

It is not justified to process the entire image at the same time as there maybe regions in the image which do not contain any useful information. By dividing the image into segments, only the important segments can be used for processing the image. That, in a nutshell, is how image segmentation works. Image segmentation is a fundamental component in numerous visual recognition systems. In the last few years, image segmentation has widely been employed in autonomous driving [31, 32], medical applications [33], agriculture sciences [34], augmented reality [35] and many more. The purpose of image segmentation is to partition images or video frames into multiple objects or segments [36]. It can be expressed as a pixel-level classification problem with semantic labels, which is known as semantic segmentation, or partitioning the images into individual objects, which is called instance segmentation [36, 37]. Semantic segmentation functions on pixel-wise labeling with a set of object categories for an image. Therefore, it is generally a more difficult task than image classification, which only predicts a single label for the entire image [37]. Furthermore, semantic image segmentation not only depends on the semantics in the question but also on the problem that needs to be addressed [38].

3   The dataset

In this work, a synthetic dataset of propagating waves in carbon fibre reinforced composite plates was computed by using the parallel implementation of the time domain spectral element method [39]. Essentially, the dataset resembles the particle velocity measurements at the bottom surface of the plate acquired by the SLDV in the transverse direction as a response to the piezoelectric (PZT) excitation at the centre of the plate. The input signal was a five-cycle Hann window modulated sinusoidal tone burst. The carrier frequency was assumed to be 50 kHz. The total wave propagation time was set to 0.75 ms so that the guided wave could propagate to the plate edges and back to the actuator twice. The number of time integration steps was 150000, which was selected for the stability of the central difference scheme.

The material was a typical cross-ply CFRP laminate. The stacking sequence $[0/90]_4$ was used in the model. The properties of a single ply were as follows [GPa]: $C_{11} = 52.55$, $C_{12} = 6.51$, $C_{22} = 51.83$, $C_{44} = 2.93$, $C_{55} = 2.92$, $C_{66} = 3.81$. The assumed mass density was 1522.4 kg/m^3. These properties were selected so that they simulated numerically wave front patterns and wavelengths that are similar to the wavefields measured by SLDV on CFRP specimens used later on for testing the developed approach for delamination identification. The shortest wavelength of the propagating A0 Lamb wave mode

was 21.2 mm for numerical simulations and 19.5 mm for experimental measurements.

475 cases were simulated, representing Lamb waves propagation and interaction with single delamination for each case. The following random factors were used in simulated delamination scenarios:

- delamination geometrical size $2b$ and $2a$, namely ellipse minor and major axis randomly selected from the interval
  $[10\,\text{mm}, 40\,\text{mm}]$,

- delamination angle α randomly selected from the interval $[0°, 180°]$,

- coordinates of the centre of delamination (x_c, y_c) randomly selected from the interval $[0\,\text{mm}, 250\,\text{mm} - \delta]$ and
  $[250\,\text{mm} + \delta, 500\,\text{mm}]$, where $\delta = 10\,\text{mm}$).

These parameters are defined in Fig. 1 which illustrates exemplary possible locations, sizes, and shapes of random delaminations used for Lamb wave propagation modeling. It should be noted that the numerical cases include delaminations located at the edge and corners of the plate.
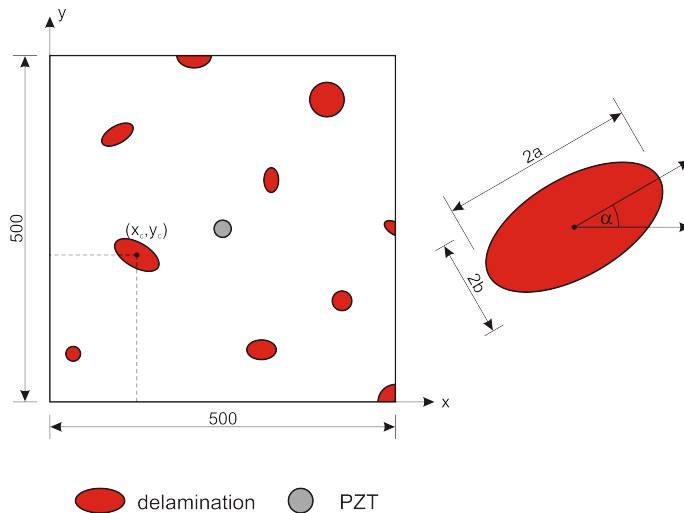

Figure 1: Exemplary locations, sizes and shapes of random delaminations used for Lamb wave propagation modeling.

The dataset contains frames of propagating waves (512 frames for each delamination scenario) and is available online [40]. The synthetic dataset is used for training the proposed neural network architecture with the aim of delamination identification directly from SLDV measurements without the need for a baseline wavefield.

Fig. 2 shows selected frames at different time-steps of the propagating Lamb waves before and after the interaction with the delamination. Frame f_1 represents the initial interactions with the delamination, which was calculated using the delamination location and the velocity of the $A0$ Lamb wave mode. While frame f_m represents the last frame in the training sequence window, accordingly, $m = 64$ for the proposed model, which will be discussed in the next section. The dataset contains 475 different cases, with 512 frames per case, producing a total number of $243,200$ frames with a frame size of (500×500) pixels representing the geometry of the specimen of size $(500 \times 500)\,\text{mm}^2$.
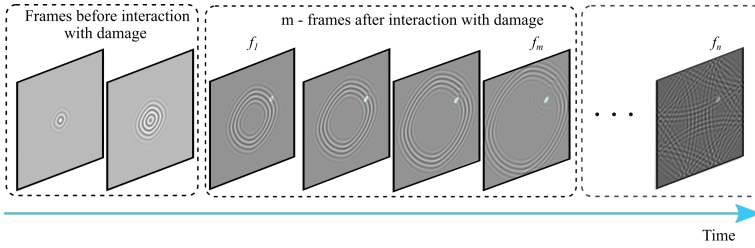
Figure 2: Sample frames of full wave propagation.

For training and evaluation of the proposed deep learning model, the dataset was divided into two sets: training and testing, with a ratio of 80% and 20% respectively. Moreover, 10% of the training set was preserved as a validation set to validate the model during the training process. Additionally, the dataset was normalised to a range of $(0,1)$ to improve the convergence of the gradient descent algorithm. The author selected 64 consecutive frames in each delamination case as using all frames in each case has high computational and memory costs. Additionally, frames displaying the propagation of guided waves before interaction with the delamination has no features to be extracted. Hence, only a certain number of frames were selected from the initial occurrence of the interactions with the delamination (see Fig. 2 for details).
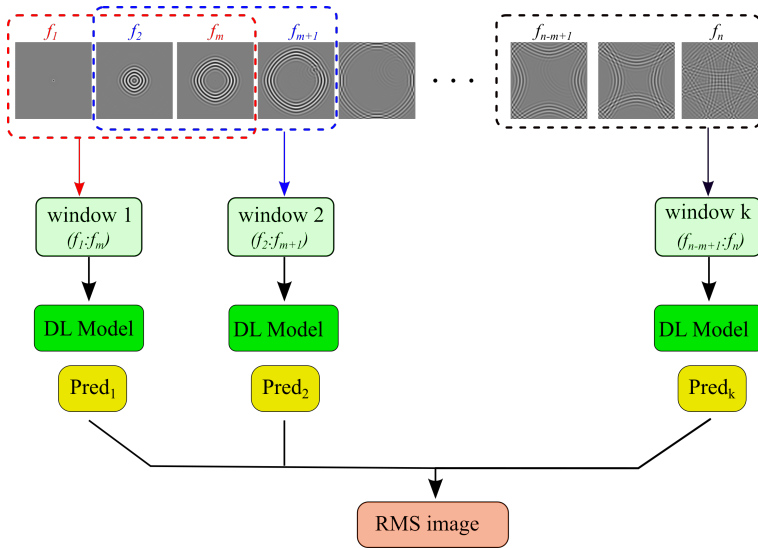

Figure 3: The procedure of calculating the RMS prediction image.

Fig. 3 illustrates the complete procedure of obtaining the intermediate predictions for the testing cases and finally calculating the RMS image. Where f_1 refers to the starting frame and f_n is the last frame, $(n = 512)$ in the dataset. Further, m refers to the number of frames in the window, which is 64 frames for the proposed model, and k represents the total number of windows. Accordingly, the author slide the window over all input frames. The shift of the window is one frame at a time.

4 Introduction to RNN, LSTM and ConvLSTM

Feed-forward neural networks such as traditional ANNs and CNNs cannot learn temporal features from the data and hence are not the best choice for sequential data processing. To handle such problems, a recurrent neural network (RNN) was introduced, which was specifically developed to address sequential data [41–43]. RNNs contain loops among the different nodes in their architecture to retain information in the model for long periods. RNNs employ the current input with the previous memory state. This ability of memory-keeping enables RNNs to predict what comes next. Furthermore, RNNs were designed to handle sequential data, which implies that updating the learnable weights must consider the extent of the time dimension. Accordingly, the backpropagation [44] algorithm responsible for updating the learnable weights needs some modification to work along with the time dimension. To alleviate this problem, backpropagation through time (BPTT) [41, 43] was introduced. Therefore, in basic RNNs, short-term memories are only preserved, so it becomes unfeasible in the case of dealing with long sequences of data. Therefore, basic RNNs usually suffer from issues like vanishing or exploding gradients in such situations [45]. Therefore, the fine-tuning of the model parameters and training of RNNs becomes very hard. To overcome such issues, Hochreiter and Schmidhuber developed the Long-Short Term Memory networks (LSTMs [46]).
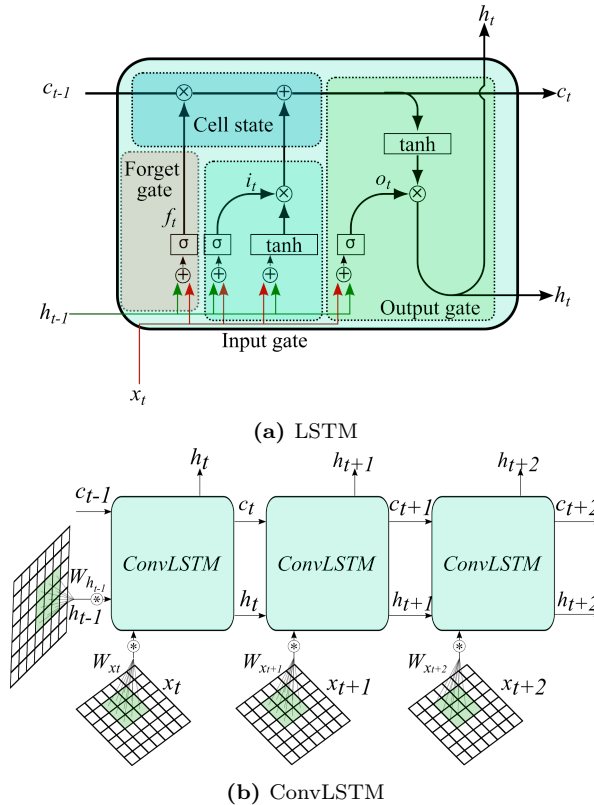

(a) LSTM

(b) ConvLSTM

Figure 4: LSTM and ConvLSTM architectures.

LSTMs were developed to keep information related to long-term dependencies and to solve the problem of vanishing and exploding gradients. Further, LSTMs handle inputs or

outputs of any length, which makes LSTMs powerful for solving very complex sequential problems. Basic LSTM architecture shown in Fig. 4a consists of four units: an input gate, a cell state, a forget gate, and an output gate. These gates help regulate the flow of information that is added to or removed from the cell state. The hidden states in LSTM hold the short-term memory, while the cells state holds the long-term memory.

The purpose of the forget gate is to decide what information to keep and what to neglect. The current input x_t and the previous hidden state h_{t-1} are passed through a sigmoid function (σ) which produce values between 0 and 1. Then the outputs of the sigmoid are multiplied with the previous cell state $c_t - 1$. Consequently, (0) outputs are discarded. The mathematical calculation at the forget gate (f_t) is depicted in Eq. (1):

$$f_t = \sigma \left(W_f \begin{bmatrix} h_{t-1} \\ x_t \end{bmatrix} + b_f \right)$$
$$W_f = \begin{bmatrix} W_{h_{t-1}} W_{x_t} \end{bmatrix}$$

(1)

where W_f represent the learnable weights at the hidden and input states h_{t-1} and x_t, respectively, and b_f represents the bias term.

The input gate i_t takes the current input x_t with the previous hidden state h_{t-1}, then applies the sigmoid function to get values in a range between 0 (not important) and 1 (important). Then, the same current input x_t, and the hidden state h_{t-1} are passed through a tanh function at the cell state ($\tilde{c}_t$) that regulate the network by transferring the values into a range between -1 and 1. Then, the outputs from the sigmoid and tanh functions are multiplied point-by-point to eliminate 0 values. Eq. (2) depicts the calculation at the input gate:

$$i_t = \sigma \left(W_i \begin{bmatrix} h_{t-1} \\ x_t \end{bmatrix} + b_i \right)$$
$$\tilde{c}_t = \tanh \left(W_c \begin{bmatrix} h_{t-1} \\ x_t \end{bmatrix} + b_c \right)$$

(2)

At this point, the network has sufficient information obtained from the input and forget gates. Hence, the current cell state c_t can be calculated by multiplying the previous cell state c_{t-1} with the output of the forget gate. Then, the result is added to the calculated input values as depicted in Eq. (3):

$$c_t = f_t \cdot c_{t-1} + i_t \cdot \tilde{c}_t$$

(3)

The output gate o_t computes the next hidden state h_t which holds information related to the current inputs. Accordingly, the current input x_t and the previous hidden state h_{t-1} are passed through a third sigmoid function to produce values between 0 and 1. The current cell state c_t is passed through a tanh function and multiplied point-by-point with o_t to produce the new hidden state h_t which is transferred to the next timestamp. Equation (4) illustrates the calculations at the output gate:

$$o_t = \sigma \left(W_o \begin{bmatrix} h_{t-1} \\ x_t \end{bmatrix} + b_o \right)$$
$$h_t = o_t \cdot \tanh(c_t)$$

(4)

where W_f, W_i, W_c and W_o have shared learnable weights.

Recently, LSTMs have been widely used for large-scale learning of language translation models, speech recognition systems, chatbots, forecasting stock markets, text data

analysis, and many more [47, 48]. However, LSTMs are inefficient at capturing spatial information by themselves when the time series inputs are consecutive images. Hence, the ConvLSTM architecture, which is a combination of CNN and LSTM units, was introduced by Shi et al. [49] to solve such kind of problems. In ConvLSTM, the convolution operations are applied both at the input-to-state transition and at the state-to-state transitions. The ConvLSTM unit, shown in Fig. 4b is a variation of the LSTM cell as it performs a convolution operation within the LSTM cell. ConvLSTM is a combination of a convolution operation and an LSTM cell. Thus, ConvLSTM can capture the time-correlated and spatial features in a series of consecutive images. Equation (5) depicts the ConvLSTM operations as the inputs $x_1, \ldots, x_t$, hidden states $h_1, \ldots, h_t$, cell states $c_1, \ldots, c_t$ and input, forget, and output gates are represented as $i_t, f_t,$ and o_t, respectively:

$$
\begin{aligned}
i_t &= \sigma \left(W_{x_t} * x_t + W_{h_{t-1}} * h_{t-1} + W_{ci} \cdot c_{t-1} + b_i \right) \\
f_t &= \sigma \left(W_{xf} * x_t + W_{hf} * h_{t-1} + W_{cf} \cdot c_{t-1} + b_f \right) \\
c_t &= f_t \cdot c_{t-1} + i_t \cdot \tanh \left(W_{xc} * x_t + W_{hc} * h_{t-1} + b_c \right) \\
o_t &= \sigma \left(W_{xo} * x_t + W_{ho} * h_{t-1} + W_{co} \cdot c_t + b_o \right) \\
h_t &= o_t \cdot \tanh \left(c_t \right)
\end{aligned}
\tag{5}
$$

where $(*)$ indicates the convolution operation, which is an element-wise multiplication operation.

Recently, ConvLSTM has become very popular and is increasingly being used in image processing applications.

5 The proposed model

In this work, the author developed an end-to-end deep learning model utilising full wavefield frames of Lamb wave propagation for delamination identification in CFRP materials. The developed model have a scheme of many-to-one sequence prediction, which takes m number of frames representing the full wavefield propagation through time and their interaction with the delamination to extract the damage features and finally predict the delamination location, shape, and size in a single output image.

The proposed model, presented in Fig. 5 takes 64 frames as input, and it consists of three ConvLSTM layers. The first ConvLSTM layer has 12 filters, the second layer has 6 filters, and the third layer has 12 filters. The kernel size of the ConvLSTM layers was set to (3×3) with a stride of (1). Padding was set to "same", which makes the output the same as the input in the case of stride 1. Furthermore, a tanh (the hyperbolic tangent) activation function was used within the ConvLSTM layers that output values in a range between $(-1$ and $1)$. Moreover, a batch normalization technique [50] was applied after the first two ConvLSTM layers.

At the final output layer, a 2D convolutional layer followed by a sigmoid activation function is applied that outputs values in a range from $(0, 1)$ to indicate the delamination probability. Consequently, a threshold value must be chosen to classify the output into damaged (represented by 1) or undamaged (represented by 0). Hence, the author set the threshold value to (0.5) to exclude all values below the threshold by considering them as undamaged and taking only those values greater than the threshold to be considered as damaged.

For evaluating the performance of the proposed model, the mean intersection over union IoU (Jaccard index) was applied as the accuracy metric. IoU is estimated by determining the intersection area between the ground truth and the predicted output.
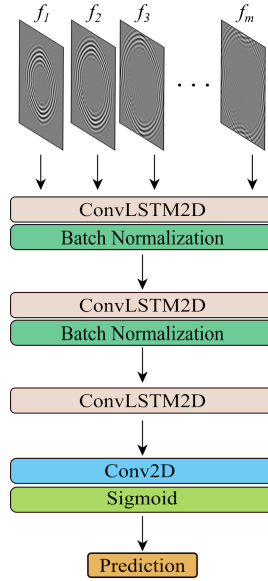
Figure 5: The architecture of the proposed deep learning model.

Further, there are two output classes (damaged and undamaged), the IoU was calculated for the damaged class only. Equation (6) illustrates the IoU metric:

$$IoU = \frac{Intersection}{Union} = \frac{\hat{Y} \cap Y}{\hat{Y} \cup Y} \tag{6}$$

where $\hat{Y}$ is the predicted output, and Y is the ground truth. Additionally, the percentage area error (ϵ) depicted in Eqn. 7 was utilised to evaluate the performance of the proposed model:

$$\epsilon = \frac{|A - \hat{A}|}{A} \times 100\% \tag{7}$$

where A and $\hat{A}$ refer to the area in mm^2 of the damage class in the ground truth and the predicted output, respectively. This metric can indicate how close the area of the predicted delamination is to the ground truth. Accordingly, the lower the value of (ϵ), the higher the accuracy of the identified damage. Furthermore, for all of the predicted outputs, the delamination localisation error (the distance between the delamination centres of the GT and the predicted output) was less than (0.001%), hence, it is not considered in the discussion section.

6 Results and discussions

In this section, the author presents the evaluation of the proposed model based on numerical data of 95 different cases representing the frames of the full wavefield propagation. The proposed model was evaluated using numerical and experimental data to demonstrate the capability to predict delamination location, shape, and size. Therefore, three representative cases were selected from the numerical dataset to show the performance of the developed model. For numerical cases, the predicted results were obtained

by using only the first window of frames after the interaction with the damage, as the delamination ground truths are provided, which is not the case for real-life scenarios as in the experimental section. Consequently, the part of producing intermediate predictions and further calculating the RMS image was skipped.

To evaluate the generalisation capability of the developed model, experimental data of single and multiple delaminations were considered. The *IoU* metric was utilised to examine the performance of the model. Furthermore, the proposed deep learning model was implemented on Keras API [51] running on top of TensorFlow on a Tesla V100 GPU from NVIDIA.

6.1 Numerical cases

In the first numerical case, the delamination is located at the upper left corner, as shown in Fig. 6a, representing its ground truth (GT). This case is considered difficult due to edge wave reflections that have similar patterns as delamination reflection.
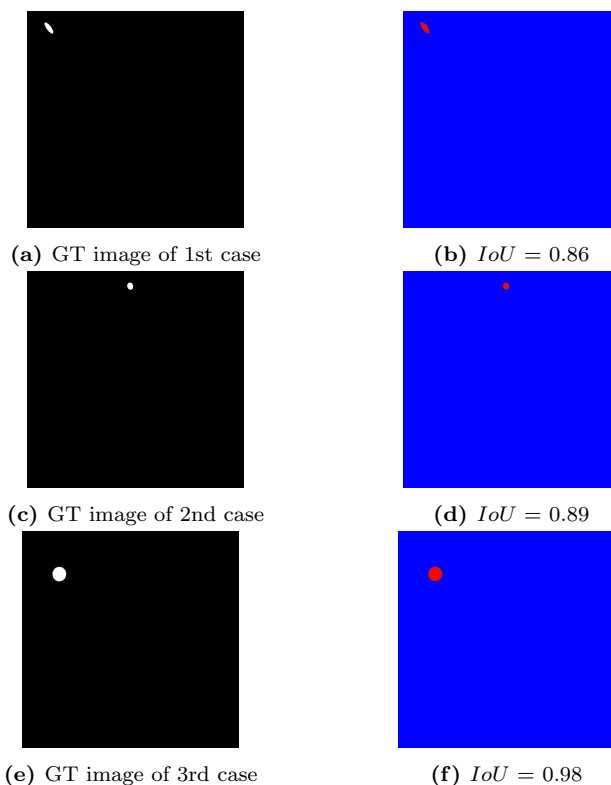

(a) GT image of 1st case

(b) $IoU = 0.86$

(c) GT image of 2nd case

(d) $IoU = 0.89$

(e) GT image of 3rd case

(f) $IoU = 0.98$

Figure 6: Delamination cases on numerical data (Figures: (a), (c), and (e) correspond to the GT of each numerical case. Figures: (b), (d) and (f) correspond to the predictions of the proposed model).

The predicted output of the first numerical case is shown in Fig. 6b. For the second numerical case, the delamination is located at the upper centre of the plate, as shown in Fig. 6c, representing the GT. This case is considered difficult due to the waves reflected from the edge have similar patterns to those reflected from the delamination. Fig. 6d shows the prediction of the second numerical case. In the third case, the delamination is

located at the upper left corner but a little farther from the edges, as shown in Fig. 6e, representing the GT. Fig. 6f shows the predicted output of the model. As can be seen in all predicted outputs, the proposed model is able to identify the delamination with high accuracy and without any noise.

Tab. 1 presents the evaluation metric of the proposed model, regarding the numerical cases shown in Fig. 6. As shown in Tab. 1, the actual (A) and predicted areas ($\hat{A}$) of delaminations were computed in mm^2 with respect to each case. The percentage area error (ϵ) was also calculated for the proposed model. The achieved mean IoU with respect to all numerical data of 95 cases was (0.90). Furthermore, the mean percentage area error (ϵ) was calculated for all numerical cases (95) was equal to 4.57%.

Table 1: Evaluation metric of the three numerical cases

Case number	A [mm^2]	IoU	$\hat{A}$ [mm^2]	ϵ
1	272	0.86	318	16.9%
2	186	0.89	196	5.4%
3	842	0.98	871	3.4%

6.2   Experimental cases

In this section, the author investigated the proposed model using experimentally acquired data. Similarly to the synthetic dataset, a frequency of 50 kHz is applied to excite a signal in a transducer placed at the centre of the plate. $A0$ mode wavelength for this particular CFRP material at such frequency is 19.5 mm. The measurements were performed by using Polytec PSV-400 SLDV on the bottom surface of the plate with dimensions of 500×500 mm. The measurements were conducted on a regular grid of 333×333 points. The measurement area was aligned with the plate edges. The sampling frequency was 512 kHz. To improve the signal-to-noise ratio, 10 averages were used. The total scanning time for one specimen was about 1h 40'. Further, a median filter using a window size of three was applied to each frame. Additionally, all frames were upsampled by using cubic interpolation to 500×500 points.

During the testing stage of the synthetic dataset, the model was fed with a consecutive number of identified frames (window of frames) containing the interactions of the Lamb waves with the delamination to identify it.

6.3   Single delamination

The first experimental case is for a CFRP specimen with single delamination created artificially by a Teflon insert of a thickness 250 μm. The complete specifications of this CFRP specimen is similar to the numerical investigations. A plain weave fabric reinforcement was used. The Teflon of a square shape was inserted during specimen manufacturing, so its shape and location are known. Based on that, the ground truth was prepared manually. Fig. 7a shows the GT image which corresponds to the artificial delamination location, shape and size. The number of the full wavefield frames is 256 frames in this case. Fig 7b shows the delamination prediction for the proposed model, and the highest IoU is (0.53) achieved for a group of frames ($35 - 99$).

Furthermore, the percentage area error metric (ϵ) was equal to 41.78%. Therefore, delamination was detected, located but its size was unidentified properly with mentioned

error. The predictions were highest for the group of frames corresponding to the first interaction of the guided waves with the delamination. Accordingly, such frames contain the most valuable feature patterns regarding delamination.
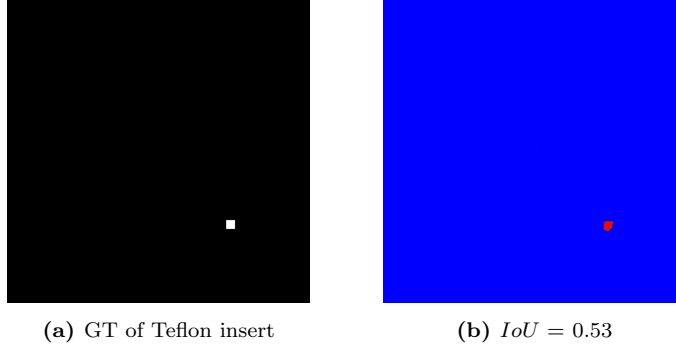

(a) GT of Teflon insert   (b) $IoU = 0.53$

Figure 7: Experimental case: single delamination of Teflon insert. (Figure (a) correspond to the GT of this experimental case. Figure (b) correspond to the predictions of the proposed model).

Furthermore, this behaviour can be depicted in Fig. 8, which shows the IoU values with respect to the predicted outputs as the author slide the window over all input frames from the starting frame till the end. Since there are 256 frames of full wavefield in this damage case, there are 192 frames of windows and has 192 consecutive predictions. Furthermore, in Fig. 8a, three places for the sliding window was selected. The first place depicted in a dark blue star shown in Fig. 8b represents a group of frames $(72 - 136)$ which correspond to the initial interaction of guided waves with the delamination. The second place is depicted in the pink pentagon shape shown in Fig. 8b represents a group of frames $(129 - 193)$ that correspond to the guided waves reflected from the edges, in which the drop in the IoU values can be noticed as these frames have fewer damage features. The third place, depicted in the green circle shown in Fig. 8b represents a group of frames $(192 - 256)$ corresponding to the interaction of the guided waves reflected from the edges with the delamination. As it can be seen, the value of IoU increases again as the valuable feature patterns regarding delamination start to appear again. The predicted outputs of the proposed model regarding the dark blue star, pink pentagon, and the green circle are shown in Fig. 9.

Additionally, for the experimental cases, the author applied the root mean square (RMS) according to Eq. 8 for all N predicted outputs $\hat{Y}$ regarding all windows of frames in order to show the damage map.

$$RMS = \sqrt{\frac{1}{N} \sum_{k=1}^{N} \hat{Y}^2} \tag{8}$$

To separate damaged and undamaged classes from the RMS images, a binary threshold with a value ($threshold = 0.5$) is applied as shown in Fig. 10a. The threshold level was selected to limit the influence of noise and at the same time highlight the damage. Fig. 10b shows the RMS image for the experimental case of single delamination predicted by the proposed model. The calculated IoU value for the case of single delamination was (0.46).
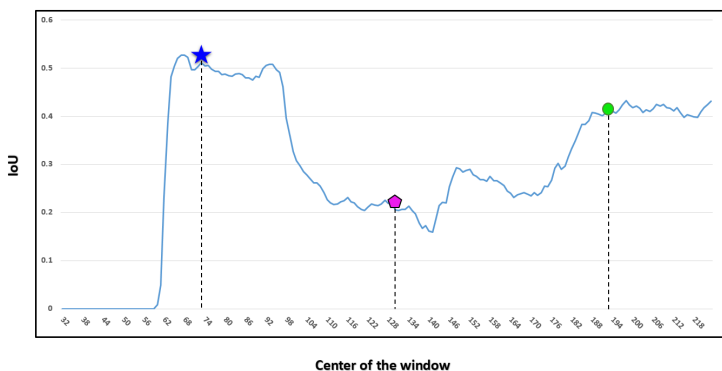
(a) IoU for the sliding window centered at consecutive frames.
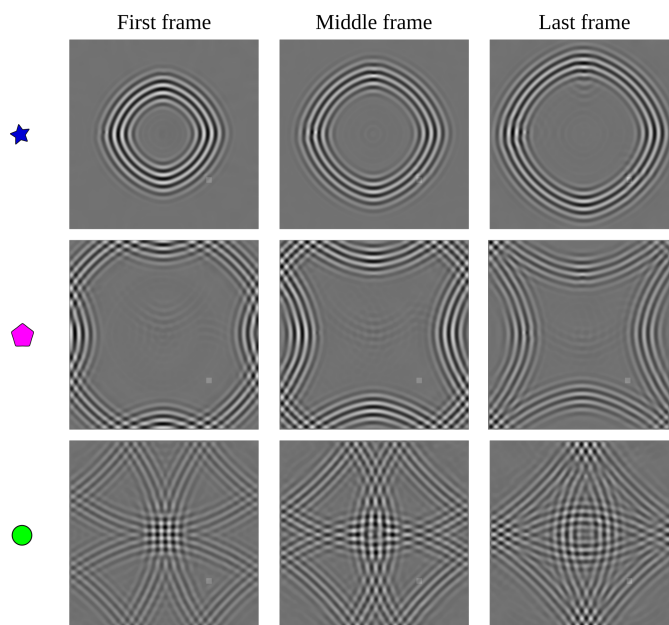
(b) Corresponding frames of guided waves.

Figure 8: IoU corresponding to a sliding window of frames (Teflon insert-single delamination).

Tab. 2 presents the evaluation metric for the proposed model, regarding the experimental case of single delamination shown in Fig. 10. As shown in Tab. 2, the actual (A) and predicted areas $(\hat{A})$ of delaminations were computed in [mm^2] with respect to each case and the percentage area error (ϵ) was calculated.

Table 2: Evaluation metric for experimental case of single delamination

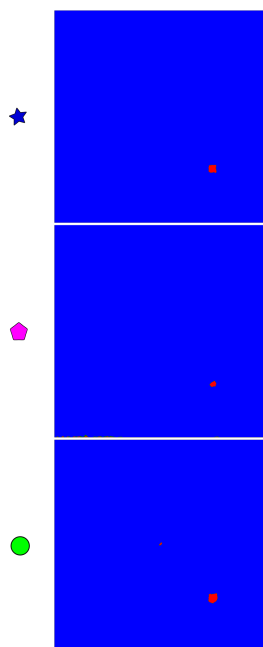| Experimental case	A [mm^2]	IoU	$\hat{A}$ [mm^2]	ϵ
Single delamination	255	0.46	319	41.78%

Figure 9: Predictions of the proposed model at different window places (Teflon insert-single delamination).
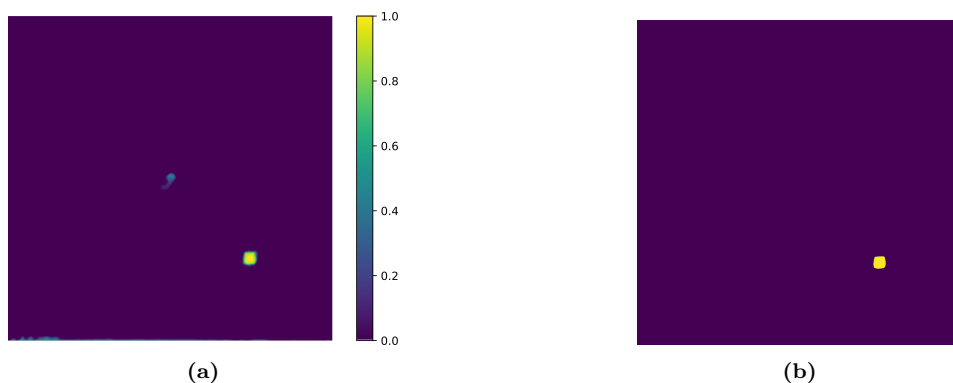

Figure 10: RMS and thresholded RMS images of predicted outputs -Teflon insert (single delamination): (a) RMS image of predicted output, (b) Thresholded RMS image of predicted output ($IoU = 0.46$)

6.4   Multiple delaminations

In the second experimental case, the author investigated three specimens of carbon/epoxy laminate reinforced by stacking sequence of 16 layers of plain weave fabric as shown in Fig. 11. Teflon inserts with a thickness of 250 μm) were used to simulate the delaminations. The prepregs GG 205 P (fibres Toray FT 300–3K 200 tex) by G. Angeloni and epoxy resin IMP503Z-HT by Impregnatex Compositi were used for the fabrication of the specimen in the autoclave. The average thickness of the specimen was 3.9 mm.

In Specimen 2, three large artificial delaminations of elliptic shape were inserted in

the upper thickness quarter of the plate between the 4th and the 5th layer. The delaminations were located at the same distance, equal to 150 mm from the centre of the plate. For Specimen 3, delaminations were inserted in the middle thickness of the plate between 8th layer and 9th layer. For Specimen 4, three small delaminations were inserted in the middle of the thickness of the plate, and three large delaminations were inserted at the lower quarter of the thickness of the plate between the 12th layer and 13th layer. The details of Specimen 2, 3 and 4 are presented in Fig. 11.

Furthermore, the SLDV measurements were conducted from the bottom surface of the plate. Consequently, Specimen 2 is the most difficult case, as the delaminations are barely visible. For Specimens (2, 3, and 4), 512 consecutive frames were generated representing the full wavefield measurements in the plate. The measurement parameters were the same as in the experiment with single delamination. Since SLDV measurements
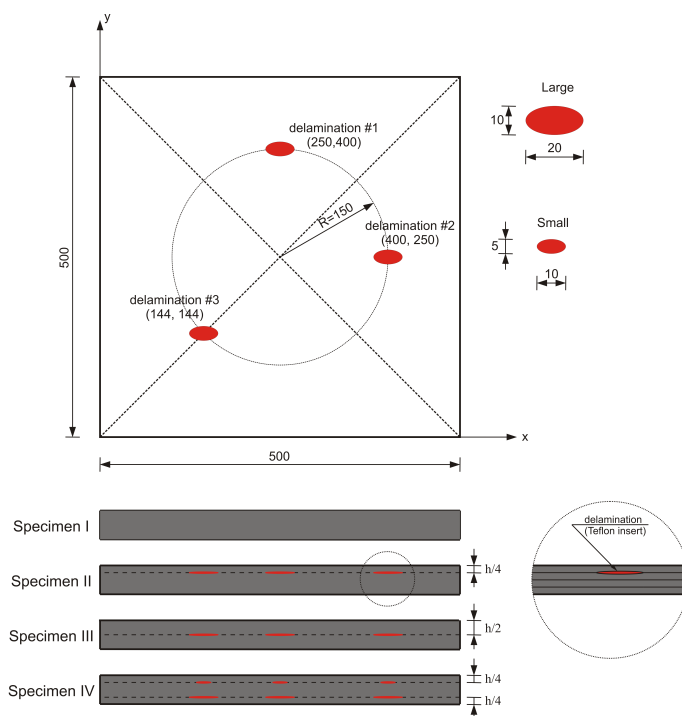

Figure 11: Experimental case of delamination arrangement.

were conducted from the bottom surface of the plate, the GT images and the output predictions of the proposed model are flipped horizontally (mirrored). Fig. 12a shows the GT image of Specimen 2. The predicted output of the proposed model is shown in Fig. 12b in which the highest calculated IoU value is 0.15 achieved for the group of frames $(167 - 231)$. Figure 12c shows the GT image of Specimen 3. The predicted output is shown in Fig. 12d in which the highest calculated IoU value is 0.18 achieved for group of frames $(279 - 343)$.

Fig. 12e shows the GT image of Specimen 4. This is assumed to be the largest delaminations in the cross-sections because the full wavefield was acquired from the bottom surface of the specimen. It is also to be noted that such a case with stacked delaminations in cross-sections was not modeled numerically (see Specimen 4 in Fig. 11). Although the model was not trained on such a scenario, the predictions were satisfactory. The predicted
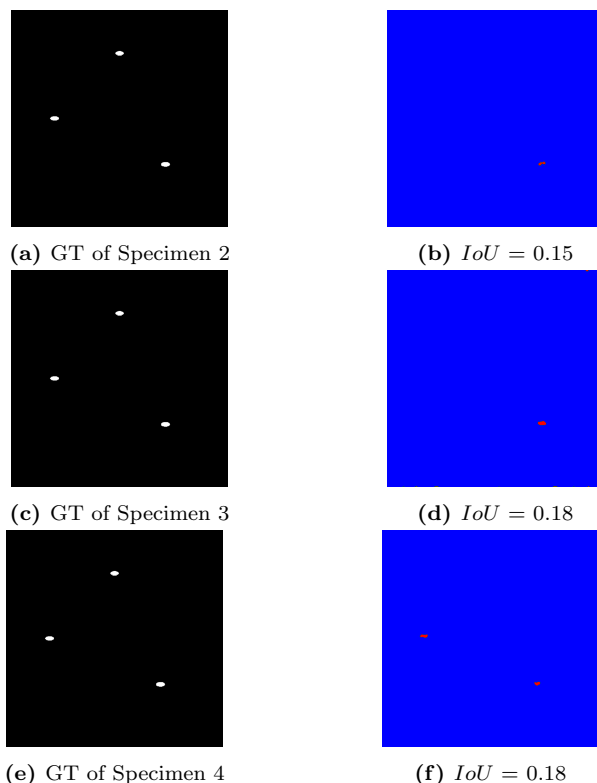
(a) GT of Specimen 2

(b) $IoU = 0.15$

(c) GT of Specimen 3

(d) $IoU = 0.18$

(e) GT of Specimen 4

(f) $IoU = 0.18$

Figure 12: Experimental cases of Specimens 2, 3, and 4. (Figures: (a), (c), and (e) correspond to the GT of each Specimen. Figures: (b), (d) and (f) correspond to the predictions of the proposed model).

output of the proposed system is shown in Fig. 12f in which the highest calculated IoU value is 0.18 achieved for the group of frames $(235 - 299)$.
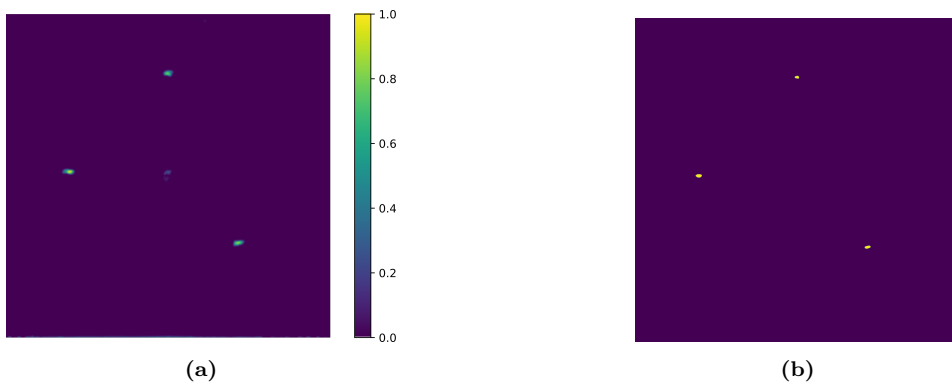

(a)

(b)

Figure 13: RMS and Thresholded RMS images of predicted outputs - Specimen 4: (a) RMS image of the predicted output, (b) Thresholded RMS image of predicted output ($IoU = 0.07$).

The RMS images depicting the damage maps of Specimen 4 are presented in Fig. 13a for the proposed model. Fig. 13b shows the thresholded RMS image for the proposed model, and the calculated value of IoU is (0.07). Furthermore, the mean percentage area error (ϵ) with respect to the three delaminations (Specimen 4) for the proposed model was equal to 79.41%.

7   Conclusions

In this work, the author presented a novel deep learning-based approach for delamination identification in composite laminates. The developed approach introduces an end-to-end scheme that performs a many-to-one sequence prediction to identify delamination location, size, and shape. Accordingly, the proposed model is trained on a consecutive number of frames depicting the full wavefield of Lamb waves propagation in a plate of CFRP, and their interactions with the delamination, and the edges. Hence, the proposed model learn how to extract the valuable features regarding the damage from such frames in order to have a prediction.

To evaluate the performance of the developed model, the author examined them on a numerical test-set that was unseen before. The results verified their ability to identify the delaminations with high accuracy. Furthermore, to evaluate the generalisation capability of the proposed model, the author tested it on several experimentally measured cases of single and multiple delaminations simulated by Teflon inserts. The predicted results are promising, considering the experimental case of multiple delaminations is difficult as the model was trained only on cases of single delamination. Consequently, the currently developed model showed its potential capability of identifying multiple delaminations at once in real-life cases.

However, there are several limitations to the SLDV measurement technique, which is used for full wavefield acquisition. The measurements constructed by using SLDV are stationary and time-consuming. Therefore, the proposed technique is more appropriate for NDT than SHM. However, it is probable that in the future, as laser technology progresses, the process of data acquisition will be possible at an array of points instead of a single point, which will considerably decrease the measurement time. It is also possible that the measurement time can be reduced by using fewer points in the spatial grid along with the compressive sensing approach. Another issue with SLDV measurements is that the laser needs access to the surface of the inspected structure, which may require partial disassembly of the structure.

The limitation related to the developed deep learning model is that the material properties of the inspected structure have to be approximately known in order to simulate the dataset for training.

Acknowledgements

References

[1] V. Giurgiutiu, "Structural health monitoring (SHM) of aerospace composites," *Polymer Composites in the Aerospace Industry*, pp. 491–558, 2019.

[2] F. Xu, Q. D. Duan Mu, L. J. Li, D. Yang, and B. Xia, "Nondestructive evaluation of rubber composites using terahertz time domain spectroscopy," *Fibres and Textiles in Eastern Europe*, vol. 26, no. 1, pp. 67–72, 2018.

[3] A. Poudel, S. S. Shrestha, J. S. Sandhu, T. P. Chu, and C. G. Pergantis, "Comparison and analysis of Acoustography with other NDE techniques for foreign object inclusion detection in graphite epoxy composites," *Composites Part B: Engineering*, vol. 78, pp. 86–94, sep 2015.

[4] R. Talreja and C. V. Singh, *Damage and failure of composite materials*. Cambridge University Press, 2012.

[5] M. R. Wisnom, "The role of delamination in failure of fibre-reinforced composites," *Philosophical Transactions of the Royal Society A: Mathematical, Physical and Engineering Sciences*, vol. 370, no. 1965, pp. 1850–1870, 2012.

[6] W. J. Staszewski, S. Mahzan, and R. Traynor, "Health monitoring of aerospace composite structures - Active and passive approach," *Composites Science and Technology*, vol. 69, no. 11-12, pp. 1678–1685, 2009.

[7] H. Tuo, Z. Lu, X. Ma, J. Xing, and C. Zhang, "Damage and failure mechanism of thin composite laminates under low-velocity impact and compression-after-impact loading conditions," *Composites Part B: Engineering*, vol. 163, pp. 642–654, 2019.

[8] R. J. Barthorpe and K. Worden, "Emerging Trends in Optimal Structural Health Monitoring System Design: From Sensor Placement to System Evaluation," *Journal of Sensor and Actuator Networks 2020, Vol. 9, Page 31*, vol. 9, p. 31, jul 2020.

[9] J. B. Ihn and F. K. Chang, "Pitch-catch active sensing methods in structural health monitoring for aircraft structures," *Structural Health Monitoring*, vol. 7, pp. 5–19, mar 2008.

[10] S. Cantero-Chinchilla, J. Chiachío, M. Chiachío, D. Chronopoulos, and A. Jones, "Optimal sensor configuration for ultrasonic guided-wave inspection based on value of information," 2020.

[11] M. Radzieński, P. Kudela, A. Marzani, L. De Marchi, and W. Ostachowicz, "Damage identification in various types of composite plates using guided waves excited by a piezoelectric transducer and measured by a laser vibrometer," *Sensors (Switzerland)*, vol. 19, p. 1958, apr 2019.

[12] D. Girolamo, H. Y. Chang, and F. G. Yuan, "Impact damage visualization in a honeycomb composite panel through laser inspection using zero-lag cross-correlation imaging condition," *Ultrasonics*, vol. 87, pp. 152–165, jul 2018.

[13] P. Kudela, M. Radzienski, and W. Ostachowicz, "Impact induced damage assessment by means of Lamb wave image processing," *Mechanical Systems and Signal Processing*, vol. 102, pp. 23–36, mar 2018.

[14] M. D. Rogge and C. A. Leckey, "Characterization of impact damage in composite laminates using guided wavefield imaging and local wavenumber domain analysis," *Ultrasonics*, vol. 53, no. 7, pp. 1217–1226, 2013.

[15] S. P. Mohanty, D. P. Hughes, and M. Salathé, "Using Deep Learning for Image-Based Plant Disease Detection," *Frontiers in Plant Science*, vol. 7, p. 1419, sep 2016.

[16] X. Zhang, L. Han, L. Han, and L. Zhu, "How Well Do Deep Learning-Based Methods for Land Cover Classification and Object Detection Perform on High Resolution Remote Sensing Imagery?," *Remote Sensing*, vol. 12, p. 417, jan 2020.

[17] M. Pashaei, H. Kamangir, M. J. Starek, and P. Tissot, "Review and Evaluation of Deep Learning Architectures for Efficient Land Cover Mapping with UAS Hyper-Spatial Imagery: A Case Study Over a Wetland," *Remote Sensing*, vol. 12, p. 959, mar 2020.

[18] R. Zhao, R. Yan, Z. Chen, K. Mao, P. Wang, and R. X. Gao, "Deep learning and its applications to machine health monitoring," *Mechanical Systems and Signal Processing*, vol. 115, pp. 213–237, 2019.

[19] D. Chakraborty, "Artificial neural network based delamination prediction in laminated composites," *Materials and Design*, vol. 26, no. 1, pp. 1–7, 2005.

[20] A. Khan, D. K. Ko, S. C. Lim, and H. S. Kim, "Structural vibration-based classification and prediction of delamination in smart composite laminates using deep learning neural network," *Composites Part B: Engineering*, vol. 161, no. August 2018, pp. 586–594, 2019.

[21] Q. Luo, B. Gao, W. L. Woo, and Y. Yang, "Temporal and spatial deep learning network for infrared thermal defect detection," *NDT & E International*, vol. 108, p. 102164, 2019.

[22] H.-T. Bang, S. Park, and H. Jeon, "Defect identification in composite materials via thermography and deep learning techniques," *Composite Structures*, vol. 246, p. 112405, 2020.

[23] Z. Su and L. Ye, "Lamb wave-based quantitative identification of delamination in CF/EP composite structures using artificial neural algorithm," *Composite Structures*, vol. 66, pp. 627–637, oct 2004.

[24] D. Chetwynd, F. Mustapha, K. Worden, J. A. Rongong, S. G. Pierce, and J. M. Dulieu-barton, "Damage localisation in a stiffened composite panel," *Strain*, vol. 44, no. 4, pp. 298–307, 2008.

[25] A. De Fenza, A. Sorrentino, and P. Vitiello, "Application of Artificial Neural Networks and Probability Ellipse methods for damage detection using Lamb waves," *Composite Structures*, vol. 133, pp. 390–403, 2015.

[26] B. Feng, D. J. Pasadas, A. L. Ribeiro, and H. G. Ramos, "Locating Defects in Anisotropic CFRP Plates Using ToF-Based Probability Matrix and Neural Networks," *IEEE Transactions on Instrumentation and Measurement*, vol. 68, no. 5, pp. 1252–1260, 2019.

[27] A. Mardanshahi, V. Nasir, S. Kazemirad, and M. M. Shokrieh, "Detection and classification of matrix cracking in laminated composites using guided wave propagation and artificial neural networks," *Composite Structures*, vol. 246, p. 112403, 2020.

[28] C. Qian, Y. Ran, J. He, Y. Ren, B. Sun, W. Zhang, and R. Wang, "Application of artificial neural networks for quantitative damage detection in unidirectional composite structures based on Lamb waves," *Advances in Mechanical Engineering*, vol. 12, no. 3, p. 1687814020914732, 2020.

[29] I. Tabian, H. Fu, and Z. S. Khodaei, "A convolutional neural network for impact detection and characterization of complex composite structures," *Sensors (Switzerland)*, vol. 19, no. 22, pp. 1–25, 2019.

[30] M. Rautela and S. Gopalakrishnan, "Ultrasonic guided wave based structural damage detection and localization using model assisted convolutional and recurrent neural networks," *Expert Systems with Applications*, vol. 167, p. 114189, 2021.

[31] G. Ros, L. Sellart, J. Materzynska, D. Vazquez, and A. M. Lopez, "The SYNTHIA Dataset: A Large Collection of Synthetic Images for Semantic Segmentation of Urban Scenes," in *Proceedings of the IEEE Computer Society Conference on Computer Vision and Pattern Recognition*, vol. 2016-Decem, pp. 3234–3243, Packt Publishing, 2016.

[32] W. Xu, B. Li, S. Liu, and W. Qiu, "Real-time object detection and semantic segmentation for autonomous driving," in *MIPPR 2017: Automatic Target Recognition and Navigation*, vol. 10608, p. 44, International Society for Optics and Photonics, Packt Publishing, 2018.

[33] S. A. Taghanaki, K. Abhishek, J. P. Cohen, J. Cohen-Adad, and G. Hamarneh, "Deep semantic segmentation of natural and medical images: a review," *Artificial Intelligence Review*, vol. 54, no. 1, pp. 137–178, 2021.

[34] A. Milioto, P. Lottes, and C. Stachniss, "Real-Time Semantic Segmentation of Crop and Weed for Precision Agriculture Robots Leveraging Background Knowledge in CNNs," in *Proceedings - IEEE International Conference on Robotics and Automation*, pp. 2229–2235, IEEE, Packt Publishing, 2018.

[35] O. Miksik, V. Vineet, M. Lidegaard, R. Prasaath, M. Nießner, S. Golodetz, S. L. Hicks, P. Pérez, S. Izadi, and P. H. Torr, "The semantic paintbrush: Interactive 3D mapping and recognition in large outdoor spaces," in *Conference on Human Factors in Computing Systems - Proceedings*, vol. 2015-April, pp. 3317–3326, Packt Publishing, 2015.

[36] R. Szeliski, *Computer vision: algorithms and applications*. Packt Publishing, 2010.

[37] S. Minaee, Y. Y. Boykov, F. Porikli, A. J. Plaza, N. Kehtarnavaz, and D. Terzopoulos, "Image segmentation using deep learning: A survey," *IEEE Transactions on Pattern Analysis and Machine Intelligence*, 2021.

[38] S. Ghosh, N. Das, I. Das, and U. Maulik, "Understanding deep learning techniques for image segmentation," *ACM Computing Surveys*, vol. 52, no. 4, pp. 1–35, 2019.

[39] P. Kudela, J. Moll, and P. Fiborek, "Parallel spectral element method for guided wave based structural health monitoring," *Smart Materials and Structures*, vol. 29, p. 095010, sep 2020.

[40] P. Kudela and A. Ijjeh, "Synthetic dataset of a full wavefield representing the propagation of Lamb waves and their interactions with delaminations," 2021.

[41] C. C. Aggarwal and Others, "Neural networks and deep learning," *Springer*, vol. 10, pp. 973–978, 2018.

[42] Y. LeCun, Y. Bengio, and G. Hinton, "Deep learning.," *Nature*, vol. 521, pp. 436–44, may 2015.

[43] I. G. Courville, Y. Bengio, and Aaron, *Deep learning*, vol. 29. MIT press Massachusetts, USA:, 2016.

[44] D. E. Rumelhart, G. E. Hinton, and R. J. Williams, "Learning representations by back-propagating errors," *Nature*, vol. 323, no. 6088, pp. 533–536, 1986.

[45] Y. Bengio, P. Simard, and P. Frasconi, "Learning long-term dependencies with gradient descent is difficult," *IEEE transactions on neural networks*, vol. 5, no. 2, pp. 157–166, 1994.

[46] S. Hochreiter and J. Schmidhuber, "Long Short-Term Memory," *Neural Computation*, vol. 9, pp. 1735–1780, nov 1997.

[47] A. Graves and N. Jaitly, "Towards end-to-end speech recognition with recurrent neural networks," in *International conference on machine learning*, pp. 1764–1772, PMLR, 2014.

[48] K. Cho, B. Van Merriënboer, D. Bahdanau, and Y. Bengio, "On the properties of neural machine translation: Encoder-decoder approaches," *arXiv preprint arXiv:1409.1259*, 2014.

[49] S. H. I. Xingjian, Z. Chen, H. Wang, D.-Y. Yeung, W.-K. Wong, and W.-c. Woo, "Convolutional LSTM network: A machine learning approach for precipitation nowcasting," in *Advances in neural information processing systems*, pp. 802–810, 2015.

[50] S. Santurkar, D. Tsipras, A. Ilyas, and A. Madry, "How does batch normalization help optimization?," in *Advances in Neural Information Processing Systems*, vol. 2018-Decem, pp. 2483–2493, 2018.

[51] F. Chollet, "Keras," 2015.